Topological Weaire–Thorpe models of amorphous matter

Quentin Marsal[a], Dániel Varjas[b,c], and Adolfo G. Grushin[a,1]

[a]Université Grenoble Alpes, CNRS, Grenoble INP, Institut Néel, 38000 Grenoble, France; [b]QuTech, Delft University of Technology, 2600 GA Delft, The Netherlands; and [c]Kavli Institute of Nanoscience, Delft University of Technology, 2600 GA Delft, The Netherlands

Edited by Andrea J. Liu, University of Pennsylvania, Philadelphia, PA, and approved October 26, 2020 (received for review April 17, 2020)

Amorphous solids remain outside of the classification and systematic discovery of new topological materials, partially due to the lack of realistic models that are analytically tractable. Here we introduce the topological Weaire–Thorpe class of models, which are defined on amorphous lattices with fixed coordination number, a realistic feature of covalently bonded amorphous solids. Their short-range properties allow us to analytically predict spectral gaps. Their symmetry under permutation of orbitals allows us to analytically compute topological phase diagrams, which determine quantized observables like circular dichroism, by introducing symmetry indicators in amorphous systems. These models and our procedures to define invariants are generalizable to higher coordination number and dimensions, opening a route toward a complete classification of amorphous topological states in real space using quasilocal properties.

amorphous solids | topological phases | symmetry indicators

Although most solids can be grown amorphous, their lack of translational symmetries has kept amorphous solids outside the recently developed topological classifications of noninteracting matter (1–3), halting their discovery for robust applications. Amorphous Bi_2Se_3 was shown to be the sole exception recently, with spectral, spin, and transport data supporting a surface Dirac cone (4). Other condensed matter platforms based on nonstoichiometric growth of the same compound are promising alternatives (5, 6), and, as a proof of principle, amorphous topological states have been realized in two-dimensional (2D) systems of coupled gyroscopes (7). However, the challenge is to model realistic materials, and determine their topological phase diagram in a way that may establish a classification and aid their systematic discovery.

Addressing this challenge seems possible, since the absence of amorphous topological solids is not fundamental; topological protection does not rely on translational invariance. This well-developed understanding dates back at least to studies of integer quantum Hall transitions (8–10). More recently, several classes of amorphous models have been shown to host integer quantum Hall (or Chern insulator) phases, as well as other topological states (7, 11–19), including numerical work that suggests differences compared to known quantum Hall transitions (19, 20). Although the corresponding topological phase diagrams can be computed numerically, by simulating responses to external fields (18) or through real space topological markers (7, 11), these methods are not generalizable to every discrete symmetry in every dimensionality. Crucially, a symmetry-based approach (21–24) for amorphous solids, which proved to be successful in high-throughput classifications of topological crystals (1–3), seems out of reach due to the absence of long-range atomic order.

In this work, we find that an overlooked yet common property of covalently bonded amorphous solids, their fixed coordination number (25), can be exploited to overcome these problems. This property is rooted in the fact that the local chemical environment in an amorphous solid is similar to that of the crystalline phase of the same compound (4, 26, 27). The local environment determines the coarse properties of the density of states such as spectral gaps, while long-range correlations or periodicity determine the finer details. Such physical input has been a cornerstone in describing amorphous states (25, 28), allowing proving of the presence of spectral gaps in amorphous Si, eventually explaining why windows are transparent (26, 28, 29). Although topological properties are nonlocal in general, and quasi-local (30) at best, this useful chemical input remains unexploited in current models of amorphous topological states.

The models we propose are an analytically tractable and generalizable set of topological amorphous models with fixed coordination. They generalize the Weaire–Thorpe Hamiltonian class (28) explicitly developed to respect the local environment across sites. We show, analytically, that they are generically gapped, and track the band crossings as a function of the parameters of the models. Remarkably, these models allow us to construct an amorphous version of symmetry indicators by exploiting the symmetry resulting from the equivalence between orbitals. We are able to map their topological phase diagram modulo an integer, without the need to compute local topological markers.

For concreteness, in this paper, we exemplify our results using a triply coordinated 2D amorphous lattice without time-reversal symmetry (7), and consider a fourfold coordinated model in *SI Appendix* that emphasizes the generality of our results. We analytically compute the spectral gaps and numerically calculate the in-gap local density of states that shows topologically protected

Significance

Topological insulators respond to external fields in fundamentally different ways compared to trivial insulators. Combining topologically robust responses with the long history of large-scale growth and broad applications of amorphous materials, a door for technological progress opens. The absence of realistic models that exploit the accumulated knowledge of both fields, and the lack of criteria to establish when topological phases emerge in amorphous solids, stalls progress. Here we propose models that are realistic and topological and display useful symmetry properties despite their lack of periodicity. They allow us to predict when amorphous topological phases occur and their physical responses, opening up a path to identify, classify, and discover amorphous topological insulators.

Author contributions: A.G.G. devised the initial concepts and theory, further developed by all authors; A.G.G. designed research; Q.M., D.V., and A.G.G. performed research; Q.M. performed the analytical calculations and implemented the numerical simulations assisted by D.V.; D.V. developed the connection to the effective Hamiltonian; Q.M., D.V., and A.G.G. contributed new analytic tools; Q.M., D.V., and A.G.G. analyzed data; A.G.G. wrote the manuscript with input from Q.M. and D.V.; and A.G.G. supervised the project.

The authors declare no competing interest.

This article is a PNAS Direct Submission.

[1]To whom correspondence may be addressed. Email: adolfo.grushin@neel.cnrs.fr.

This article contains supporting information online at https://www.pnas.org/lookup/suppl/doi:10.1073/pnas.2007384117/-/DCSupplemental.

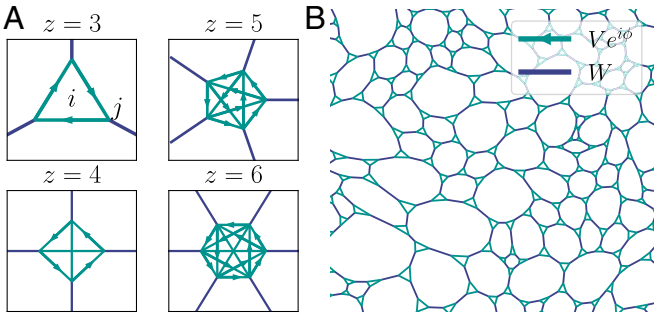

Fig. 1. Topological Weaire–Thorpe models. (*A*) Basic building blocks for threefold, fourfold, fivefold, and sixfold coordinated Weaire–Thorpe models. The diagrams show a single site i with z orbitals labeled by j. The green lines indicate the intrasite hopping $Ve^{i\phi}$, while the blue lines are the intersite hopping W. (*B*) Example of a threefold coordinated topological Weaire–Thorpe model.

edge states. We numerically compute the local Chern marker (30), which we link to a quantized circular dichroism, mapping the topological phase diagram in parameter space. We then introduce the symmetry indicators for this model and combine them in a formula that delivers the Chern number modulo three (modulo four in the case of fourfold coordination), reproducing the topological phase diagram analytically. Finally, for the threefold coordinated model, we discuss to what extent an effective Hamiltonian approach (31), that projects the full Hamiltonian into a basis of plane waves, can also detect topological phase transitions.

Due to their gapped structure and previous success in describing amorphous solids, the models we propose are natural candidates to describe realistic amorphous topological insulators and to track their topological phase transitions. Moreover, there is no fundamental restriction to extend our analytical arguments to different dimensionality, symmetry classes, and coordination number, hinting at a route to classify amorphous topological insulators.

Results

Topological Weaire–Thorpe Model Class. Irrespective of dimensionality and coordination, we define the topological Weaire–Thorpe models by a Hamiltonian with two terms, $H_{\mathrm{WT}} = H_V + H_W$, defined by

$$H_{\mathrm{WT}} = \sum_{i,j\neq j'}^{z} V_{jj'}^{(i)} \left|i,j\right\rangle \left\langle i,j'\right| + \sum_{i\neq i',j}^{z} W_{ii'}^{(j)} \left|i,j\right\rangle \left\langle i',j\right|. \quad [1]$$

The index i labels sites within a z coordinated lattice, while $j = 1, 2, \ldots z$ labels the z orbitals within a site (Fig. 1*A*). The matrices $V_{jj'}^{(i)}$ connect different orbitals within a single site, while the matrices $W_{ii'}^{(j)}$ connect different sites through a single pair of orbitals such that coordination remains fixed. If the intrasite and intersite matrices are chosen real and independent of i and j, respectively, such that $V_{jj'}^{(i)} = V \in \mathrm{Re}\ \forall i, j \neq j'$ and $W_{ii'}^{(j)} = W \in \mathrm{Re}\ \forall i \neq i', j$, Eq. **1** reduces to the Weaire–Thorpe model, introduced to describe spectral properties of tetravalent ($z = 4$) amorphous materials such as amorphous Si (28). The form of Eq. **1** is motivated by the experimental observation that covalently bonded amorphous materials conserve the local environment imposed by their individual components, resembling their crystalline counterparts at short scales (25). Lattice disorder emerges at larger scales, modifying the lattice structure compared to the crystal (Fig. 1*B*).

To define the topological Weaire–Thorpe model, here, we allow V to be complex, respecting that the local environment of different orbitals remains equivalent. This imposes that V should be invariant with respect to cyclic permutation of the orbitals, and that the hopping between sites is fixed to W, which we keep real. These requirements do not fix the orientation of the complex phases of V, a freedom that can be adjusted depending on the physical context we wish to describe (see Fig. 1*A* for a specific convention and *SI Appendix*, section B for further discussion). Given a convention for these complex phases, the fixed coordination will allow us to show that Weaire–Thorpe models have spectral gaps in general and determine their band edges analytically.

To show the existence of spectral gaps of the topological Weaire–Thorpe model and determine where they occur, we use the resolvent method (32), outlined next and described in detail in *SI Appendix*, section C. It is based on the observation that the eigenvalues of the system are poles of the complex function

$$\varepsilon \mapsto \frac{1}{\varepsilon - H_V - H_W} = \frac{1}{\varepsilon - H_V} \sum_{n=0}^{+\infty} \left(\frac{H_W}{\varepsilon - H_V}\right)^n, \quad [2]$$

known as the resolvent of the Hamiltonian. If the series converges for a given ε, then ε is not a pole of the resolvent and therefore not an eigenvalue of the Hamiltonian. A sufficient condition for convergence is that

$$\left\| \frac{H_W}{\varepsilon - H_V} \right\| < 1, \quad [3]$$

where $\|\cdot\|$ is the operator norm, equal to the maximum absolute eigenvalue. Hence, we can determine the energy windows where there are no states, the spectral gaps, as a function of the model parameters with the condition $\min_{\lambda \in Sp(H_V)} |E - \lambda| > W$ where λ spans the z eigenvalues of H_V, $Sp(H_V)$. Although true for all V and W, the criterion Eq. **3** is useful as long as W is less than the distance separating two eigenvalues of H_V, but it is not very informative when $W \gg V$. In this latter case, it is more instructive to use the freedom to interchange the roles of H_V and H_W in the last step of Eq. **2**. In this case, we arrive at the second condition $\min(E \pm W - \overline{V}) > \max_{\lambda \in Sp(H_V)}(|\lambda - \overline{V}|)$, where $\overline{V}$ is a real number introduced to minimize $\|H_V - \overline{V}\|$. The combination of these inequalities constrains the energy regions where there are no states, the spectral gaps. For generic W, V, and coordination z, these gaps are finite, and therefore the topological Weaire–Thorpe models describe an insulator at fillings where the chemical potential lies within the spectral gap. The gap boundaries are determined analytically by these inequalities, a useful property that we will use to determine the topological phase diagram.

Threefold Coordinated Weaire–Thorpe–Chern Insulator. As an illustration of the power of the Weaire–Thorpe models, we now construct a 2D Hall insulator in an amorphous lattice with coordination $z = 3$ and determine its electromagnetic responses and topological phase diagram numerically and analytically (see *SI Appendix*, section F for the case $z = 4$). With the building block labeled $z = 3$ in Fig. 1*A*, we first build a threefold coordinated lattice by making use of a Voronization procedure (*SI Appendix*, section D). A specific realization of this lattice is shown in Fig. 1*B*. As indicated by Fig. 1*A*, we keep $W \in \mathrm{Re}$ and promote $V \to Ve^{i\phi}$, choosing the phases to connect in a clockwise fashion.

As anticipated, the structure of the Weaire–Thorpe model allows prediction of band gaps analytically. Applying our

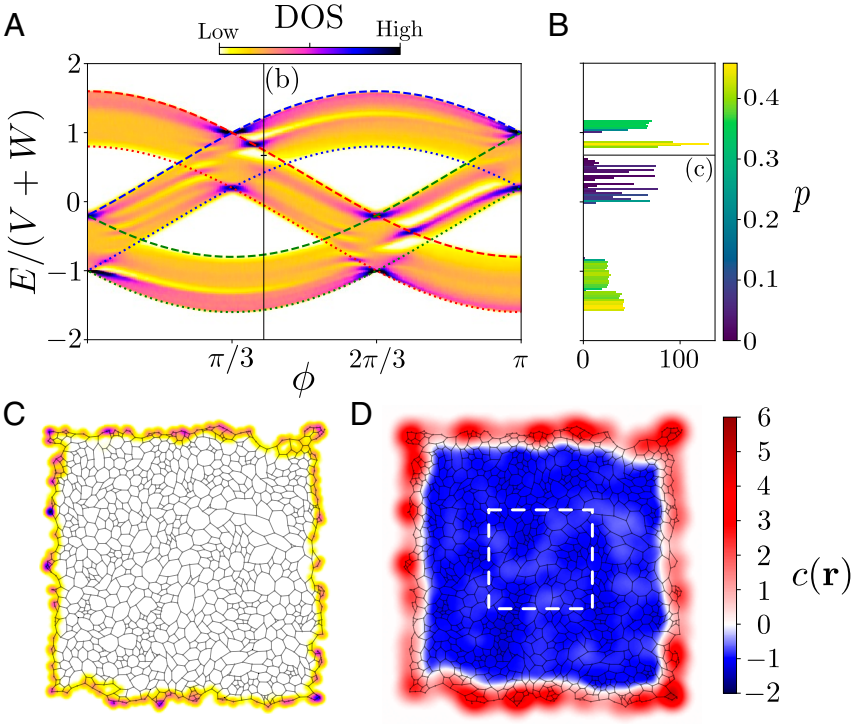

Fig. 2. Spectral properties. (*A*) The energy spectrum for $W/V = 0.66$ as a function of ϕ with periodic boundary conditions. The color intensity is proportional to the density of states (DOS). The dashed and dotted lines are obtained from the resolvent inequalities Eq. **4**, and correspond to states with $F_+ = 1$ and $F_- = 1$, respectively (Fig. 3*D*). Their color coding follows that of Fig. 3*C*. The vertical line $\phi = 1.3$ indicates the parameters chosen for *B*–*D*. (*B*) The color bar shows the participation ratio $p = (\sum_i |\psi_i|^2)^2 / N|\psi_i|^4$ for periodic boundary conditions, a measure of localization that indicates the ratio of sites contributing to the density of states within a given energy bin. The height of the histogram is proportional to the density of states. (*C*) The local density of states with open boundary conditions for an in-gap state at 2/3 filling indicated by the black line in *B*, showing the edge support of in-gap states. (*D*) The local Chern marker density $c(\mathbf{r})$ at 2/3 filling, quantized to $C = -1$ in the bulk, with a large and positive edge contribution, typical of a Chern insulating phase. The white dashed square shows the averaging region used to compute Fig. 3*A*.

general criteria above, we can determine the band edges and spectral gaps through the inequality

$$\left| E - 2\,V\cos\left(\phi + m\frac{2\pi}{3}\right)\right| < |\,W\,|, \qquad [4]$$

with $m = 0, \pm 1$. As discussed later, the different values of m label the C_3 rotation eigenstates of H_V (see also *SI Appendix*, section D).

In Fig. 2*A*, we compare the energy spectrum as a function of ϕ calculated numerically using periodic boundary conditions and the Kernel Polynomial Method (33), with the spectrum outlined by the inequalities Eq. **4**. The lines set by Eq. **4** match exactly with the band edges of the numerical spectrum. The agreement confirms Weaire and Thorpe's original expectation: The local environment of a site is enough to determine the broad spectral features, and where the gap closures appear (28). Our goal is to show that these properties also allow us to determine the topological phase diagram.

To do so, we first show that the model can be, indeed, topologically nontrivial and discuss some of its physical properties. With open boundary conditions, we observe that states appear within bulk gaps for certain values of parameters. A typical local density of states of these in-gap states is shown in Fig. 2*C*. The wave functions of these states are localized at the edge, suggestive of a topological edge mode.

To map the topological phase diagram, and predict physical properties, we have calculated the local Chern marker $\mathcal{C}(\mathbf{r})$ at each lattice site $\mathbf{r}$ for different parameter values. The local Chern marker can be regarded as the real space counterpartof the Berry curvature (30, 34). It is defined at each site as the expectation value (*SI Appendix*, section A)

$$\mathcal{C}(\mathbf{r}) = 2\pi \mathrm{Im}\,\langle \mathbf{r}|\left[\hat{Q}\hat{x}, \hat{P}\hat{y}\right]|\mathbf{r}\rangle\,, \qquad [5]$$

over localized states $|\mathbf{r}\rangle$, where $\hat{P}$ and $\hat{Q}$ are projectors onto the occupied and unoccupied eigenstates.

With periodic boundary conditions, and for a 2D insulator, the density of the local Chern marker is equal to the total Chern number, $C = \mathrm{Tr}[\mathcal{C}(\mathbf{r})]/A_{\mathrm{sys}}$, where A_{sys} is the area of the system (30, 34). With open boundary conditions, $\mathrm{Tr}[\mathcal{C}(\mathbf{r})] = 0$, since it is the trace of a commutator in a finite Hilbert space (34–36). In an atomic insulator, $\mathcal{C}(\mathbf{r})$ is zero on all $\mathbf{r}$, resulting in a vanishing trace over all sites. In contrast, when the Chern number is finite, the area-averaged $\mathcal{C}(\mathbf{r})$ in the bulk takes an integer value that equals C, which is compensated exactly by an edge contribution of opposite sign upon averaging over all sites. The local Chern marker thus serves to diagnose topology of 2D insulators without time-reversal symmetry.

Using the Chern marker, we can compute the topological phase diagram, shown in Fig. 3*A*, for the representative case of 2/3 filling. It features three phases with Chern numbers $C = 0, \pm 1$, shown for $\phi \in [0, \pi]$, since $C(\phi) = -C(-\phi)$. To visualize quantization in Fig. 2*D*, we plot the dimensionless local Chern marker density (34) $c(\mathbf{r})$ within the topological state with $C = -1$ at $\phi = 1.3$. By definition (*SI Appendix*, section A), $c(\mathbf{r})$ coincides with the density of $\mathcal{C}(\mathbf{r})$, on average, converging to C upon summing over bulk sites. The edge state contribution, with opposite sign, is clearly visible.

The local Chern marker is a tool to elucidate the topological phase diagram of this model, but is also connected to

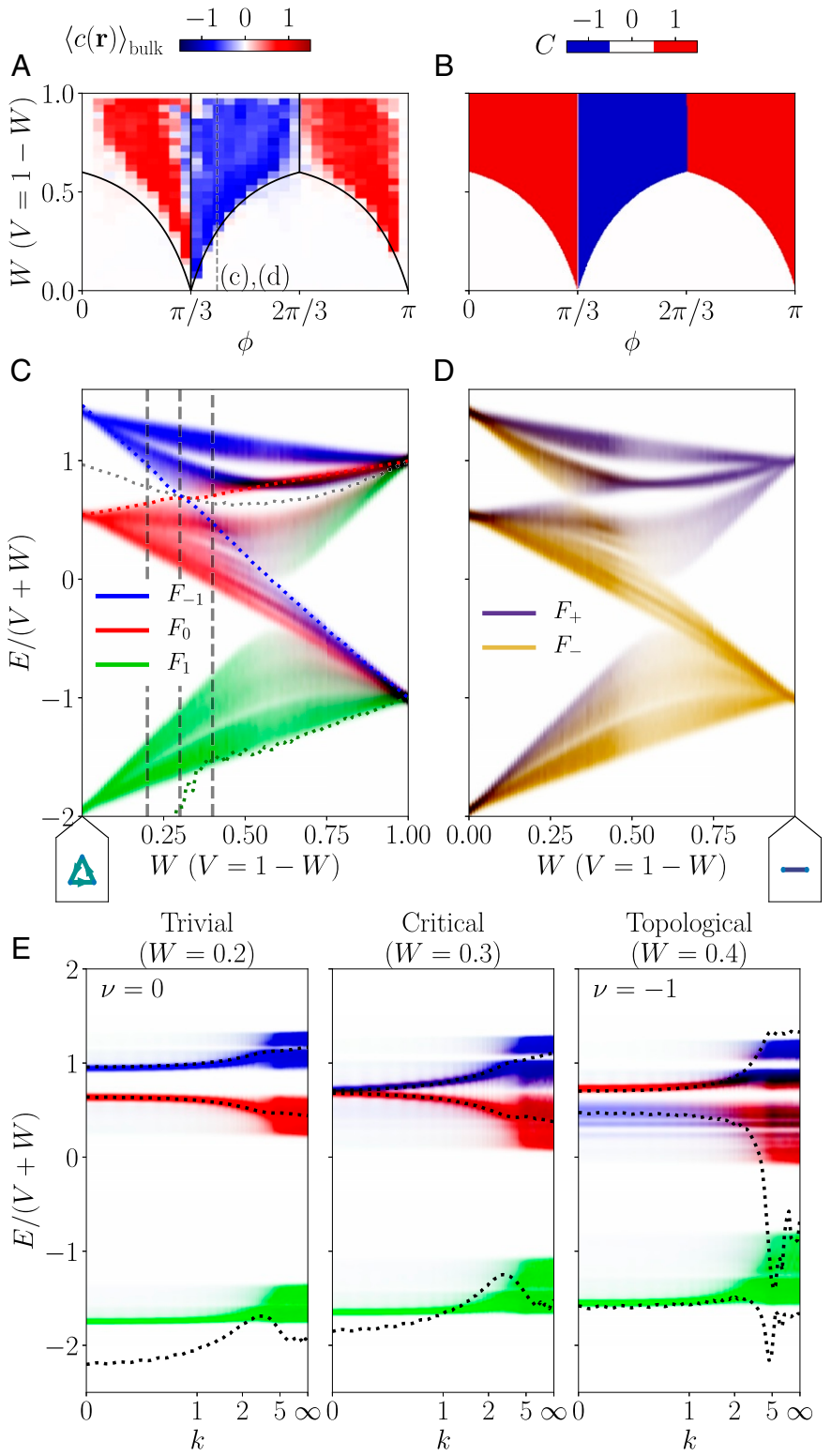

Fig. 3. Topological phase diagram and symmetry properties of the $z=3$ Weaire–Thorpe model at $\nu=2/3$ filling. (*A*) Topological phase diagram obtained from the local Chern marker density averaged over the area within the dashed white square in Fig. 2*D*, $\langle c(\mathbf{r})\rangle_{\text{bulk}}$. The solid lines indicate the gap closing transitions obtained using the inequalities Eq. **4**. The vertical dashed line indicates $\phi=1.3$, used in *C* and *D*. (*B*) Topological phase diagram using the symmetry indicator formula Eq. **6**. (*C*) Spectral densities $F_m(E)$. We use an RGB color value to visualize how a given eigenstate transforms under C_3 rotations (see *Symmetry Indicators and Topological Invariants*). The dotted lines show the effective Hamiltonian spectrum at $\mathbf{k}=0$ for $l=0,\pm1$ with the same color coding. The gray dotted line indicates a 2/3 filling. The vertical dashed lines indicate $W=0,2$, $W=0,3$, $W=0,4$ used in *E*. The *Lower Left* schematic shows the trivial decoupled triangle limit ($W=0$). (*D*) Spectral densities $F_\pm(E)$. We use a two-color coding to visualize how a given eigenstate transforms under bond inversion (see *Symmetry Indicators and Topological Invariants*). The *Lower Right* schematic shows the trivial dimer limit ($V=0$). (*E*) Momentum resolved spectral weights $F_m(E,\mathbf{k})$ showing a band inversion at $|\mathbf{k}|\equiv k=0$. The eigenvalues of $H_{\text{eff}}(\mathbf{k})$ are shown as dark dotted lines. The red, green, and blue colors correspond to $m=0,1,-1$ respectively. The continuum Chern number ν changes from $\nu=0$ to $\nu=-1$ across the transition.

physical properties. Firstly, the Hall conductivity σ_{xy} is determined by the Chern number, $\sigma_{xy} = Ce^2/h$. Secondly, $\mathrm{Tr}[\mathcal{C}(\mathbf{r})]$ determines the absorption rate difference between driving the system with left- and right-handed circularly polarized electric field of amplitude E (35). This observation does not rely on translational invariance, and thus our model should show a quantized circular dichroism. By following ref. 35, we show that the differential frequency-integrated absorption rate is quantized to $\Delta\Gamma/A_{\mathrm{sys}} = E^2\hbar^2\mathrm{Tr}[\mathcal{C}\ (\mathbf{r})]/A_{\mathrm{sys}} = E^2\hbar^2 C$ (*SI Appendix*, section A). A finite quantized circular dichroism can be measured even for finite samples, upon integrating to frequencies up to the band gap (36).

Symmetry Indicators and Topological Invariants. By construction, the Weaire–Thorpe models impose that all orbitals are equivalent. We show, next, how we can use the resulting underlying symmetries, cyclic permutation of the orbitals on a site ($2\pi/z$ rotations) and bond inversion, to determine the topological phase diagram. For concreteness, we consider the $z = 3$ case in the following, but our conclusions carry over to the general case with minimal modifications.

The properties of the eigenstates of H_{WT} under rotations are best understood starting from the trivial limit $W = 0$. In this limit, Eq. **1** defines a set of decoupled triangles, each governed by H_V (Fig. 3*C*, *Lower Left* schematic). The system is topologically trivial, since it is possible to form a basis of localized states (37, 38). Its spectrum consists of three bands with $N/3$ states each, where N is the total number of orbitals in the system. Therefore, fillings $N/3$ and $2N/3$ define trivial insulators. Since H_V is invariant under $2\pi/3$ rotations, the local site symmetry group is C_3. This implies that, at $W = 0$, all states are exact eigenstates of C_3, labeled by their rotation eigenvalues $w_m = e^{i2\pi m/3}$ with $m = 0, \pm 1$.

Crucially, the eigenstates of the Hamiltonian H_{WT} at the band edges determined by Eq. **4** remain eigenvectors of H_V whatever the relative magnitude of V, W, and ϕ (see *SI Appendix*, section D for an analytical derivation). For general states, we characterize the transformation properties under threefold rotations by computing $F_m(|\psi\rangle) = \sum_i |\langle i, m|\psi\rangle|^2$, the overlap with the eigenvectors $|i, m\rangle$ of H_V localized on site i. With respect to C_3, $|i, 0\rangle$ transforms as an s-like orbital with eigenvalue $w_0 = 1$, while $|i, \pm 1\rangle$ transform as $p_x \pm ip_y$-like orbitals with eigenvalues $w_{\pm 1} = e^{\pm i2\pi/3}$. For any state, $F_m \geq 0$ and $\sum_m F_m = 1$, so we assign an RGB color code to visualize how it transforms under C_3 rotations (Fig. 3*C*). As advertised, states at the band edges have $F_m(|\psi\rangle) = 1$ for some m and are exact C_3 eigenstates.

Similarly, to understand the properties of the eigenstates of H_{WT} under inversion, we start from the $V = 0$ limit. When $V = 0$, the system is a set of decoupled dimers (Fig. 3*D*, *Lower Right* schematic). The energy spectrum is composed of two bands at energies $\pm W$, with $N/2$ states each, labeled by ± 1 bond inversion eigenvalues. At $1/2$ filling, the system is a trivial insulator. Analogous to our procedure above, we characterize the properties of any eigenstate under inversion away from $V = 0$ by introducing $|j, \pm\rangle$, the eigenvectors of H_W localized on the dimer j, and computing $F_\pm(|\psi\rangle) = \sum_j |\langle j, \pm|\psi\rangle|^2$. As before, the band edges remain eigenstates of H_W whatever the relative magnitude of V, W, and ϕ (*SI Appendix*, section D), which can be seen in Fig. 3*D*.

Since band edges remain eigenvectors of H_V and H_W separately, and these track band crossings, it is suggestive that, using Eq. **4**, we can track changes in Chern numbers. This would allow mapping of a topological phase diagram analytically. To this end, we take inspiration from the idea of symmetry indicators (21–24) (see ref. 39 for a review), and extend those developed for Chern insulators (40). Relevant to our analysis, the latter work established, in particular, that, in 2D crystals with C_n rotational symmetry, the Chern number can be determined modulo n by multiplying rotation eigenvalues of filled states. This multiplication amounts to summing the exponents, m_p, of the filled rotation eigenvalues of C_3, as $\sum_p \ldots$. We then observe that the Chern number at a given point in the phase diagram can be computed as

$$C\,(\mathrm{mod}\,3) = \sum_{p\in\mathrm{filled}} m_p - \sum_{p\in\mathrm{filled}} m_p^{W=0}. \qquad [6]$$

The second term in this expression acts as a reference for the trivial state, which is well defined for 1/3 and 2/3 fillings, while the first tracks band inversions. For $2/3$ filling, the resulting phase diagram is shown in Fig. 3*B*. It reproduces that computed from the local Chern marker (Fig. 3*A*), yet its computation is analytical. A similar invariant can be found for $z = 4$ as shown in *SI Appendix*, section F.

It is appealing to connect the success of the invariant Eq. **6** to known topological invariants. First, Eq. **6** can be thought of as the amorphous analogue of the Chern number equation formula for crystals with C_3 symmetry (40). Second, in continuous media, the Chern number can be computed by subtracting angular momentum eigenvalues l of filled states at $|\mathbf{k}| \equiv k = 0$ and $k = \infty$ (41, 42), by defining $\nu = \sum_{n\in\mathrm{filled}} l_n(k = 0) - l_n(k = \infty)$. The $k = \infty$ term captures the short-distance properties, and thus it is suggestive to interpret it as the second term in Eq. **6**. Similarly, the $k = 0$ term captures long-distance properties, and it is tempting to identify it with the first term in Eq. **6**. Although appealing, this identification is subtle, because, even in crystals, further neighbor hoppings can break the naive intuition that gap inversions occur at $k = 0$. Therefore, establishing a formal correspondence is an interesting open problem, yet the similarities between ν and Eq. **6** and the average rotational symmetry of amorphous lattices suggest that ν can be used to signal amorphous topological states.

To investigate this possibility, we extend a recent description of topological quasicrystalline phases (31) to our amorphous lattices. By projecting the real space Hamiltonian into a basis of plane waves with a given $\mathbf{k}$, we can define an effective Hamiltonian in momentum space, $H_{\mathrm{eff}}(\mathbf{k})$ (31). Since this procedure does not rely on translational symmetry, we define $H_{\mathrm{eff}}(\mathbf{k})$ for our amorphous system using a basis of angular momentum states (*SI Appendix*, section E).

The symmetry properties of $H_{\mathrm{eff}}(\mathbf{k})$ allow us to compute ν and compare it to Eq. **6**. As $k = 0$ and $k = \infty$ are invariant under continuous rotations, the eigenstates of $H_{\mathrm{eff}}(k = 0)$ and $H_{\mathrm{eff}}(k = \infty)$ can be labeled by their angular momentum l. The colored dotted lines in Fig. 3*C* show the eigenstates of $H_{\mathrm{eff}}(0)$ labeled by $m = l \in [-1, 0, 1]$, which closely follow the spectral densities $F_m(E)$. The $l = 0$ and $l = -1$ eigenvalues of $H_{\mathrm{eff}}(0)$ cross at the first topological phase transition, while the eigenvalues of $H_{\mathrm{eff}}(\infty)$ maintain the same ordering. This behavior matches that of the momentum-resolved spectral densities of the permutation eigenstates $F_m(E, \mathbf{k})$ (Fig. 3*E*) which also present a band inversion at $k = 0$ across the topological transition. For general $\mathbf{k}$, the eigenstates of $H_{\mathrm{eff}}(\mathbf{k})$ disperse, but remain gapped and continuous, establishing a connection to regularized continuum Hamiltonians (41, 42). By explicitly computing the invariant ν, that compares the number of filled angular momentum eigenstates at $k = 0$ and ∞, we can establish the topological character of this band inversion, which changes $\nu = 0$ to $\nu = -1$. However, we find that this approach only results in a meaningful $H_{\mathrm{eff}}(\mathbf{k})$ sufficiently close to the decoupled triangle limit $W/V \lesssim 1$, capturing only part of the phase diagram (see *SI Appendix*, section E for a discussion).

Discussion

We have proposed a class of realistic models with fixed coordination that allow analytical tracking of topological phase transitions

in amorphous lattices. These models are motivated by the observation that the local environment of a site is similar in the crystalline and amorphous lattices, the latter lacking long-range order. A fixed coordination allows us to show that these models are generically gapped, and the equivalence between orbitals allows us to assign a symmetry label to band edges. Treating these labels as symmetry indicators, we have constructed the topological index (6), successfully reproducing the topological phase diagram of a threefold Weaire–Thorpe–Chern insulator analytically. We have linked the phase diagram to physical responses, predicting that 2D amorphous models with broken-time reversal symmetry present a quantized circular dichroism, similar to their crystal counterparts (35). The topological index (6) can be defined for any z, signaling a way to determine the phase diagram of any 2D Weaire–Thorpe model in the Altland–Zirnbauer class A analytically. Since local topological markers are only defined for topological classes with $\mathbb{Z}$ invariants (43, 44), our symmetry indicators could serve as an alternative proxy of topological phases.

Our results are a promising step to incorporate symmetries, such as orbital equivalence or average rotational symmetry, to classify amorphous topological states beyond the 10-fold way. These could be combined with the effective Hamiltonian approach (31) and with extra symmetries, such as time-reversal or particle-hole symmetry, to answer the question of whether new topological states, absent in crystals, can exist in amorphous matter. One way that new phases can appear is by considering local building blocks with symmetries absent in crystals, such as C_5 or C_8 rotations. It is interesting to speculate whether these symmetries could lead to unexpected quantum Hall transitions in amorphous 2D magnetic materials. Lastly, our models admit easy generalizations to higher dimensions and nonhermitian couplings.

Our work establishes that, in the absence of translational invariance, it is possible to construct topological models that incorporate realistic elements, such as fixed coordination, and for which the topological phase diagram can be computed analytically using symmetry, contrary to naive expectation. They are therefore natural candidates to describe amorphous topological states in the solid state (4), and they can serve as models for synthetic systems, such as photonic Chern bands, where large optical gaps can be realized using continuous random networks (45, 46).

Data Availability. Code data have been deposited in Zenodo (DOI: 10.5281/zenodo.3741829).

1. M. G. Vergniory *et al.*, A complete catalogue of high-quality topological materials. *Nature* **566**, 480–485 (2019).
2. T. Zhang *et al.*, Catalogue of topological electronic materials. *Nature* **566**, 475–479 (2019).
3. F. Tang, H. C. Po, A. Vishwanath, X. Wan, Comprehensive search for topological materials using symmetry indicators. *Nature* **566**, 486–489 (2019).
4. P. Corbae *et al.*, Evidence for topological surface states in amorphous Bi_2Se_3. arXiv:1910.13412 (29 October 2019).
5. M. Dc *et al.*, Room-temperature high spin–orbit torque due to quantum confinement in sputtered BixSe(1–x) films. *Nat. Mater.* **17**, 800–807 (2018).
6. P. Sahu *et al.*, Room temperature Mott hopping and second harmonic characterization of amorphous Gd-alloyed Bi2Se3. arXiv:1911.03323 (8 November 2019).
7. N. P. Mitchell, L. M. Nash, D. Hexner, A. M. Turner, W. T. M. Irvine, Amorphous topological insulators constructed from random point sets. *Nat. Phys.* **14**, 380–385 (2018).
8. J. T. Chalker, P. D. Coddington, Percolation, quantum tunnelling and the integer Hall effect. *J. Phys. C Solid State Phys.* **21**, 2665–2679 (1988).
9. H. P. Wei, D. C. Tsui, A. M. M. Pruisken, Localization and scaling in the quantum Hall regime. *Phys. Rev. B* **33**, 1488–1491 (1986).
10. B. Huckestein, Scaling theory of the integer quantum Hall effect. *Rev. Mod. Phys.* **67**, 357–396 (1995).
11. A. Agarwala, V. B. Shenoy, Topological insulators in amorphous systems. *Phys. Rev. Lett.* **118**, 236402 (2017).
12. M. Xiao, S. Fan, Photonic chern insulator through homogenization of an array of particles. *Phys. Rev. B* **96**, 100202 (2017).
13. K. Pöyhönen, I. Sahlberg, A. Weststrom, T. Ojanen, Amorphous topological superconductivity in a Shiba glass. *Nat. Commun.* **9**, 2103 (2018).
14. C. Bourne, E. Prodan, Non-commutative Chern numbers for generic aperiodic discrete systems. *J. Phys. Math. Theor.* **51**, 235202 (2018).
15. A. Agarwala, V. Juricic, B. Roy, Higher order topological insulators in amorphous solids. arXiv:1902.00507 (1 February 2019).
16. Y. B. Yang, T. Qin, D. L. Deng, L. M. Duan, Y. Xu, Topological amorphous metals. *Phys. Rev. Lett.* **123**, 076401 (2019).
17. M. Costa, G. R. Schleder, M. B. Nardelli, C. Lewenkopf, A. Fazzio, Toward realistic amorphous topological insulators. *Nano Lett.* **19**, 8941–8946 (2019).
18. P. Mukati, A. Agarwala, S. Bhattacharjee, Topological and conventional phases of a three-dimensional electronic glass. *Phys. Rev. B* **101**, 035142 (2020).
19. I. Sahlberg, A. Weststrom, K. Pöyhönen, T. Ojanen, Topological phase transitions in glassy quantum matter. *Phys. Rev. Research* **2**, 013053 (2020).
20. M. N. Ivaki, I. Sahlberg, T. Ojanen, Criticality in amorphous topological matter – beyond the universal scaling paradigm. arXiv:2006.05886 (10 June 2020).
21. J. Kruthoff, J. de Boer, J. van Wezel, C. L. Kane, R. J. Slager, Topological classification of crystalline insulators through band structure combinatorics. *Phys. Rev. X* **7**, 041069 (2017).
22. H. C. Po, A. Vishwanath, H. Watanabe, Symmetry-based indicators of band topology in the 230 space groups. *Nat. Commun.* **8**, 50 (2017).
23. B. Bradlyn *et al.*, Topological quantum chemistry. *Nature* **547**, 298–305 (2017).
24. Z. Song, T. Zhang, Z. Fang, C. Fang, Quantitative mappings between symmetry and topology in solids. *Nat. Commun.* **9**, 3530 (2018).
25. R. Zallen, *The Physics of Amorphous Solids* (Wiley, 1998).
26. D. Weaire, Existence of a gap in the electronic density of states of a tetrahedrally bonded solid of arbitrary structure. *Phys. Rev. Lett.* **26**, 1541–1543 (1971)
27. C. T. Toh *et al.*, Synthesis and properties of free-standing monolayer amorphous carbon. *Nature* **577**, 199–203 (2020).
28. D. Weaire, M. F. Thorpe, Electronic properties of an amorphous solid. I. A simple tight-binding theory. *Phys. Rev. B* **4**, 2508–2520 (1971).
29. M. F. Thorpe, D. Weaire, R. Alben, Electronic properties of an amorphous solid. III. The cohesive energy and the density of states. *Phys. Rev. B* **7**, 3777–3788 (1973).
30. R. Bianco, R. Resta, Mapping topological order in coordinate space. *Phys. Rev. B* **84**, 241106 (2011).
31. D. Varjas *et al.*, Topological phases without crystalline counterparts. *Phys. Rev. Lett.* **123**, 196401 (2019).
32. L. Schwartz, H. Ehrenreich, Comment on the tight-binding model for amorphous semiconductors. *Phys. Rev. B* **6**, 4088–4090 (1972).
33. A. Weiße, G. Wellein, A. Alvermann, H. Fehske, The kernel polynomial method. *Rev. Mod. Phys.* **78**, 275–306 (2006).
34. R. Bianco, "*Chern invariant and orbital magnetization as local quantities,*" PhD thesis, Università degli studi di Trieste, Trieste, Italy (2014).
35. D. T. Tran, A. Dauphin, A. G. Grushin, P. Zoller, N. Goldman, Probing topology by "heating": Quantized circular dichroism in ultracold atoms. *Sci. Adv.* **3**, e1701207 (2017).
36. O. Pozo, C. Repellin, A. G. Grushin, Quantization in chiral higher order topological insulators: Circular dichroism and local chern marker. *Phys. Rev. Lett.* **123**, 247401 (2019).
37. D. J. Thouless, Wannier functions for magnetic sub-bands. *J. Phys. C Solid State Phys.* **17**, L325–L327 (1984).
38. A. A. Soluyanov, D. Vanderbilt, Wannier representation of $\mathbb{Z}_2$ topological insulators. *Phys. Rev. B* **83**, 035108 (2011).
39. H. C. Po, Symmetry indicators of band topology. arXiv:2002.09391 (21 February 2020).
40. C. Fang, M. J. Gilbert, B. A. Bernevig, Bulk topological invariants in noninteracting point group symmetric insulators. *Phys. Rev. B* **86**, 115112 (2012).
41. T. Van Mechelen, Z. Jacob, Quantum gyroelectric effect: Photon spin-1 quantization in continuum topological bosonic phases. *Phys. Rev.* **98**, 023842 (2018).
42. T. Van Mechelen, Z. Jacob, Nonlocal topological electromagnetic phases of matter. *Phys. Rev. B* **99**, 205146 (2019).
43. I. Mondragon-Shem, T. L. Hughes, J. Song, E. Prodan, Topological criticality in the chiral-symmetric AIII class at strong disorder. *Phys. Rev. Lett.* **113**, 046802 (2014).
44. J. Song, E. Prodan, AIII and BDI topological systems at strong disorder. *Phys. Rev. B* **89**, 224203 (2014).
45. M. Florescu, S. Torquato, P. J. Steinhardt, Designer disordered materials with large, complete photonic band gaps. *Proc. Natl. Acad. Sci. U.S.A.* **106**, 20658–20663 (2009).
46. M. Rechtsman *et al.*, Amorphous photonic lattices: Band gaps, effective mass, and suppressed transport. *Phys. Rev. Lett.* **106**, 193904 (2011).